Heliyon 10 (2024) e35400

Contents lists available at ScienceDirect

Heliyon

journal homepage: www.cell.com/heliyon

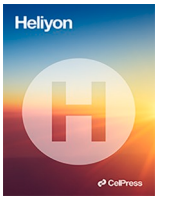

Research article

Fabrication and catalytic activity of TiO_2/Fe_3O_4 and Fe_3O_4/β-cyclodextrin nanocatalysts for safe treatment of industrial wastewater

Safer Tale Almutairi

Department of Chemistry, College of Science, University of Hafr Al Batin, P.O. Box 1803, Hafr Al Batin 39524, Saudi Arabia

ARTICLE INFO

Keywords:
Nanocatalyst
Fe_3O_4
TiO_2
β-cyclodextrin
Heavy metals
Wastewater

ABSTRACT

The rapid industrial growth has led to increased production of wastewater containing pollutants like heavy metals and organic compounds. These pollutants pose risks to human health and the environment if not properly treated. Engineered nanocatalyst materials (ENMs) are a burgeoning technology that show promise for treating industrial wastewater. Metal oxide ENMs, such as Fe_3O_4@β-cyclodextrin and Fe_3O_4@TiO_2, have demonstrated efficient removal of heavy metals and methylene blue from wastewater. Fe_3O_4@TiO_2 was found to be more effective than Fe_3O_4@β-cyclodextrin in removing these pollutants. The highest removal efficiencies were observed at a concentration of 40 mg/g and pH 8. Copper showed the highest removal efficiency (160.5 mg/g), followed by nickel (77.09 mg/g), lead (56.0 mg/g), and cadmium (46.05 mg/g). For methylene blue, the highest removal efficiency was also observed at a concentration of 40 mg/g and pH 8 (91.16 %). Lead (90.5 %), copper (90.48 %), nickel (83.34 %), and cadmium (77.58 %) were also efficiently removed. These findings highlight the potential of Fe_3O_4@TiO2 as a promising material for industrial wastewater treatment, offering cleaner and safer water for human health and the environment. ENMs have the potential to revolutionize wastewater treatment processes.

1. Introduction

Untreated wastewater poses a significant global environmental challenge, with an estimated 80 % of effluent lacking proper treatment and reuse. This issue directly impacts 1.8 billion people who rely on water sources contaminated with harmful microbes and pathogens [1]. The aquaculture industry, known for its high-water consumption, further exacerbates this problem by generating substantial wastewater containing heavy metals, non-degradable materials, and organic pollutants [2]. These challenges necessitate the development of effective and environmentally friendly purification methods for sustainable wastewater treatment.

Advanced oxidation processes (AOPs) have emerged as a promising solution to address these water contamination issues. AOPs generate highly reactive hydroxyl radicals (OH•) for effective decontamination while producing minimal toxic byproducts [3,4]. Nanomaterials, with their unique properties, have significantly enhanced the efficiency of AOPs in wastewater treatment. Nanophotocatalysts, in particular, have gained considerable attention due to their chemical stability, economic viability, and abundant availability. Their layered band gap structure, strong light absorption, and optimized band edges for catalysis facilitate efficient pollutant degradation and contribute to groundwater purification [5].

Among various nanomaterials, iron oxide nanoparticles (NPs) and titanium dioxide (TiO_2) have shown great promise in

E-mail address: stalmutairi@uhb.edu.sa.

https://doi.org/10.1016/j.heliyon.2024.e35400
Received 11 December 2023; Received in revised form 6 July 2024; Accepted 29 July 2024
Available online 29 July 2024
2405-8440/© 2024 Published by Elsevier Ltd. This is an open access article under the CC BY-NC-ND license (http://creativecommons.org/licenses/by-nc-nd/4.0/).

photocatalytic applications. Iron oxide NPs offer low cost, low toxicity, and unique magnetic properties, making them attractive for catalytic applications [6]. TiO_2, known for its chemical stability and effectiveness as a photocatalyst, has garnered significant interest in addressing environmental problems [7]. Environmentally synthesized Fe_2O_3 and TiO_2 nanoparticles have demonstrated efficacy in photocatalysis applications, with Fe_2O_3 showing decontamination effectiveness against methylene blue (MB) and TiO_2 efficiently removing Zn(II) and Pb(II) from water [8].

Recent advancements in nanocomposite materials have further expanded the potential for addressing water contamination challenges. Studies have explored various nanocomposites, such as ZnO–Fe_3O_4/TiO_2, which demonstrated superior photocatalytic degradation of Reactive Blue 21 dye compared to MIL-125(Ti) [9]. Environmentally friendly synthesis methods have produced nanocomposites like γ-Fe_2O_3/MWCNT/Ag from waste materials, showing high sulfamethazine adsorption capacity and antibacterial activity [10]. Another eco-friendly nanoadsorbent, γ-Fe_2O_3/MWCNTs/Cellulose, derived from waste tires and natural cellulose, exhibited efficient malachite green removal from aqueous solutions, following pseudo-second-order kinetics and the Langmuir isotherm model [11].

As research in this field continues to advance, the development of more efficient and environmentally friendly nanomaterials for wastewater treatment holds great promise for addressing global water contamination challenges and promoting sustainable water management practices. The integration of these innovative materials and technologies into advanced oxidation processes and photocatalytic systems offers a path forward in tackling the pressing issue of untreated wastewater and its impact on global health and environmental sustainability.

2. Material and methods

2.1. Samples

All of the chemicals and reagents were acquired from Sigma Aldrich (Burlington, MA, USA) and utilized at a high level of purity (>99 %). Industrial wastewater samples were randomly collected from the main effluent sources of three ceramic factories, prior to the water entering their respective treatment units. The samples were obtained using specialized containers designed for this purpose. Subsequently, the physical and chemical properties of the wastewater were analyzed at room temperature. The analysis revealed the following characteristics: a pH value of 6.12, indicating a slightly acidic nature; Total Dissolved Solids (TDS) of 547.78 mg/L; Electrical Conductivity (EC) of 1472.06 μS/cm; and a Conductivity measurement of 121.43 mS/cm. These measurements provide a comprehensive profile of the untreated industrial wastewater, serving as a baseline for subsequent treatment processes and efficacy evaluations.

Following the synthesis of all nanomaterials and the preparation of formulations 1 and 2, comprehensive characterization measurements were conducted to analyze their chemical and physical properties. Adsorption experiments were then performed using varying concentrations of the nanocomposites. For both nanocompost 1 (Fe_3O_4@β-cyclodextrin) and nanocompost 2, concentrations of 20 mg/L, 30 mg/L, and 40 mg/L were tested. The experimental procedure involved mixing 20 mg of nanocomposite 1 with 1000 mL of sample solution, stirring at 200 rpm for 1.5 h at ambient temperature under sunlight exposure. The solution's pH was adjusted using phosphoric acid or sodium hydroxide as needed. Heavy metal concentrations were determined before and after treatment using inductively coupled plasma optical emission spectroscopy (ICP-OES). The adsorption capacity was calculated using the equation: Adsorption capacity (mg/g) = [(Co - Ce)/m] × V, where Co is the initial concentration (μg/mL), Ce is the concentration after treatment, m is the adsorbent mass, and V is the solution volume containing the solute.

2.2. Synthesis of Fe_3O_4 magnetic nanoparticles

Fe_3O_4 magnetic nanoparticles were synthesized using the co-precipitation method, following the procedure described by Ref. [12]. A 3:2 M ratio of Fe^{3+} to Fe^{2+} was employed, with tetraethylammonium hydroxide (0.3 mol L^{-1}) serving as the precipitating agent. The process began by dissolving 0.015 M each of iron (II) chloride tetrahydrate ($FeCl_2 \bullet 4H_2O$) and iron (III) chloride hexahydrate ($FeCl_3 \bullet 6H_2O$) in 100 mL of deionized water under vigorous stirring and nitrogen protection. Tetraethylammonium hydroxide solution (0.3 M) was then slowly added to the mixture until a pH of 11 was reached. The reaction mixture was maintained at 50 °C for 30 min under continuous stirring, followed by heating at 80 °C for 1 h. Finally, the resulting Fe_3O_4 magnetic nanoparticles were washed several times with deionized water to remove any residual tetraethylammonium hydroxide, yielding the purified nanoparticles for further use.

2.3. Synthesis of (Fe_3O_4/TiO_2) nanocomposites

A two-step process was employed to synthesize the nanocomposite material. In the first step, a homogeneous mixture A was prepared by combining 0.1 g of Fe_3O_4 nanoparticles with 4 mL of titanium isoperoxide (TIP) as the titanium source, and 70 mL of water. This mixture was subjected to ultrasonic treatment in a water bath for 1 h. Concurrently, a homogeneous mixture B was prepared by mixing 3 mL of acetic acid with 90 mL of distilled water. In the second step, solution B was added to solution A and stirred at 50 °C for 30 min. The resulting solid material was then separated from the suspension via centrifugation, rinsed with ethanol, and dried at 70 °C for 6 h. The final step involved heating the dried solid under atmospheric pressure at 300 °C for 1 h, yielding the desired nanocomposite material.

2.4. Synthesis of Fe_3O4@ β-CD

To synthesize the Fe_3O_4@β-cyclodextrin nanocomposite, a precise procedure was followed. Initially, 2 g of β-cyclodextrin (CD) was dissolved in 100 mL of distilled water. Subsequently, a co-precipitation method was employed using Fe^{3+} and Fe^{2+} ions in a 3:2 M ratio. $FeCl_3 \cdot 6H_2O$ (5 g) and $FeCl_2 \cdot 4H_2O$ (2 g) were slowly added to the CD solution and vigorously stirred at 80 °C until a clear solution was obtained. Aqueous ammonia was then added to adjust the pH to 11–12, followed by continued vigorous stirring at 80 °C for an additional 30 min. The resulting precipitate was collected using an external magnet, washed multiple times with water and methanol, and dried in a vacuum oven at 60 °C for 6 h. The dried solid was then dispersed in water, and its pH was adjusted to 5 using hydrochloric acid. After 30 min of stirring, the final product was washed with water in the presence of an external magnet, yielding the Fe_3O_4@β-cyclodextrin nanocomposite.

2.5. Synthesis TiO_2

The synthesis of ideal TiO_2 powder was achieved through the preparation of titanium citrate, utilizing a reaction between citric acid and titanium (IV) isopropoxide at a fixed molar ratio of 3:1. The process began by dissolving citric acid in water under increased stirring at approximately 70 °C. Titanium isopropoxide was then gradually added to the solution in 10 mL increments while maintaining the temperature and agitation conditions. This careful addition resulted in the formation of a clear, stable titanium citrate solution. The mixture was continuously stirred for several hours to ensure complete reaction and homogeneity. Following this extended stirring period, the solution was filtered to remove any undissolved particles or impurities. The final step involved gravimetric determination of the titanium content as TiO_2, providing a quantitative measure of the synthesized product.

2.6. TEM (transmation electron microscope)

The morphological characteristics, including size and shape, of the nanomaterials synthesized in this study (Fe_3O_4 and TiO_2) were directly observed and analyzed using Transmission Electron Microscopy (TEM). The TEM imaging was conducted using equipment manufactured by JEOL (U.K.) LTD., England.

2.7. XRD (X-ray diffractometer)

The crystalline phase composition of the synthesized nanomaterials was quantitatively determined using Rietveld analysis, performed with an X-ray diffractometer (PA Nalytical B.V. Almelo, the Netherlands). The diffraction data were collected using Cu-Kα radiation with a wavelength (λ) of 0.154060 nm. The measurement parameters were optimized for high-resolution data acquisition, with a step time of 10 s, a step size of 0.05°, and a 2θ angular range spanning from 5° to 95°.

2.8. Thermogravimetric analyzer (TGA)

Thermal analysis of the samples was conducted using a Shimadzu thermogravimetric analyzer DTG-60 H equipped with TA 60 software (Tokyo, Japan). Aluminum oxide served as the reference material. Experiments were performed in platinum crucibles, with samples heated up to 1000 °C under varying heating rates (5, 10, 15, and 20 °C min^{-1}) in a dry nitrogen atmosphere flowing at 20 mL min^{-1}. For each experiment, approximately 3 mg of sample was used.

2.9. Fourier transform infrared spectroscopy (FTIR)

Fourier Transform Infrared (FTIR) spectroscopy analysis was conducted using a Shimadzu IR-460 Spectrometer to characterize the functional groups present in the synthesized nanomaterials. Sample preparation involved thoroughly mixing 50 mg of the sample with 200 mg of potassium bromide (KBr). This mixture was then compressed under high pressure to form a thin, transparent pellet suitable for FTIR analysis. A background spectrum was collected using a pellet made solely of anhydrous KBr to ensure accurate baseline correction.

2.10. ICP-OES (inductively coupled plasma optical emission spectroscopy)

The quantitative analysis of selected heavy metals, including cadmium (Cd), lead (Pb), cobalt (Co), copper (Cu), and nickel (Ni), was performed using Inductively Coupled Plasma Optical Emission Spectroscopy (ICP-OES). The instrument employed for this purpose was a Thermo Scientific iCAP 6000 Series ICP-OES, manufactured by Thermo Fisher Scientific (Cambridge, UK).

2.11. UV–vis spectrophotometer

The concentration of methylene blue dye (MBD) in the samples was determined using UV–visible spectrophotometry. A Jenway 6850/115V double beam UV–vis spectrophotometer was employed for this analysis. Measurements were taken at a wavelength of 664 nm, which corresponds to the maximum absorption peak of methylene blue. A calibration curve was constructed using standard solutions of known concentrations, allowing for the accurate quantification of MBD in the experimental samples.

3. Result and discussion

3.1. Characterization of nanomaterial

The physicochemical properties of Fe_3O_4 nanoparticles were characterized via TEM imaging (Fig. 1A and B). The images of the synthesized magnetite nanoparticles revealed a cubic shape with an average particle size of 12.7 nm.

TEM imaging of TiO_2 (anatase) nanoparticles revealed a spherical shape, with an average particle size of 25 nm.

3.2. X-ray diffraction (XRD)

The X-ray diffraction (XRD) pattern of TiO_2/Fe_3O_4 shows that the anatase TiO_2 phase is the predominant crystalline phase present in the composite. The peaks are located at 25.2°, 37.7°, 48.1°, 53.8°, 55.2°, and 62.6° corresponding to the (101), (004), (200), (105), (211) and (204) planes, respectively (Fig. 2).

The X-ray diffraction (XRD) analysis provided critical insights into the structural characteristics of the synthesized nanocomposites. For TiO_2/Fe_3O_4, the results confirmed the successful TiO_2 coating while preserving the Fe_3O_4 phase structure [13]. The peak positions and intensities aligned well with standard XRD patterns for Fe_3O_4 (JCPDS card No. 01–1111) [14], maghemite and magnetite (JCPDS card No. 39–1346) [15], TiO_2 anatase (JCPDS card no. 21–1272) [16], and TiO_2 rutile (JCPDS card no. 21–1276) [17]. The Fe_3O_4@β-CD composite exhibited significant γ-Fe_2O_3 diffraction peaks, indicating successful surface modification of iron oxide nanoparticles. The lower peak intensity compared to pure Fe_3O_4 suggested the embedding of Fe_3O_4 within the amorphous β-CD structure, further corroborated by the presence of β-CD diffraction peaks at specific 2θ positions (15.6°, 22.22°, 26.3°, 29.44°, 31.5°, 39.6°, 47.1°, 52.4°, and 55.3°). This β-CD pattern aligns with the cage-like molecular structure [18]. Overall, the XRD patterns confirmed the successful synthesis of both TiO_2/Fe_3O_4 and Fe_3O_4@β-CD composites, with the former showing anatase TiO_2 phase and the latter exhibiting γ-Fe_2O_3 phase, providing valuable information about their phase structure and morphology.

3.3. FTIR

The FTIR Spectrum of the TiO_2-coated sample showed a shift in peaks from 668 to 693 cm^{-1} to 710 and 780 cm^{-1}, respectively (Fig. 3). These peaks are attributed to the vibration modes of Fe–O and Ti–O–Ti, respectively, indicating the presence of both TiO_2 and Fe_3O_4 in the *m*-TiO2/Fe_3O_4 sample. The FTIR spectrum is consistent with the data provided in the image. The peak at 3490 cm^{-1} corresponds to the O–H bonds of β-cyclodextrin. The peaks at 3200 cm^{-1} and 1770 cm^{-1} are attributed to the C–H stretching vibration and the C–C stretching vibration of glucose molecules units (Oligosaccharide), respectively.

The peak at 1491 cm^{-1} is attributed to the C=O stretching vibration of the ester group. The peak at 1180 cm^{-1} is corresponds to the asymmetric stretching vibration of the C–O– C bond. The peaks at 710 cm^{-1}, 780 cm^{-1}, and 860 are attributed to the Fe–O bond, Ti–O–Ti bond, and Ti–O–C bond, respectively. The FTIR spectrum and the data provided in the image are consistent with the presence of both TiO_2 and Fe_3O_4 in the TiO_2/Fe_3O_4 sample [19].

The FTIR spectrum exhibited a broad band in the 500–700 cm^{-1} region, characteristic of Ti–O–Ti stretching vibrations. The broadness of this band can be attributed to the overlapping of Ti–O and Fe–O peaks, suggesting the successful incorporation of both titanium and iron oxides in the nanocomposite structure. This observation aligns with previous studies on similar materials [20]. Furthermore, the spectrum revealed distinctive peaks associated with β-cyclodextrin, as reported by Banisharif et al. (2013) and Sakinah and Rohaida (2009) [21,22]. These peaks include C–H bending at 690 cm^{-1}, C–C bending vibrations at 644 cm^{-1}, and C–H stretching vibrations for substituted aromatic compounds at 695 cm^{-1}. The presence of these characteristic β-cyclodextrin peaks confirms its successful integration into the nanocomposite structure, providing strong evidence for the synthesis of the Fe_3O_4@β-CD composite and corroborating the findings of previous studies in the field [20–22].

3.4. TGA

TGA results revealed distinct thermal behaviors for the two compositions, Fe_3O_4@β-CD and Fe_3O_4/TiO_2 (Fig. 4). For Fe_3O_4@β-CD, a 7 % weight loss occurred between 50 and 140 °C due to water evaporation and decomposition of residual solvents in the

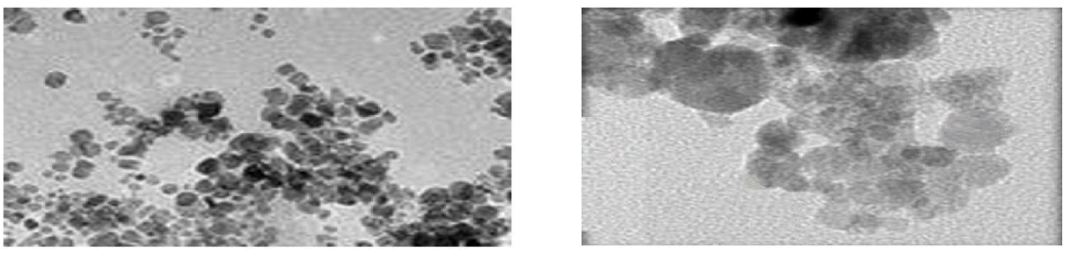

Fig. 1. (A&B): TEM imaging of the prepared NPs revealed the shape of the particles, with an average size for Magnetite and titanium dioxide.

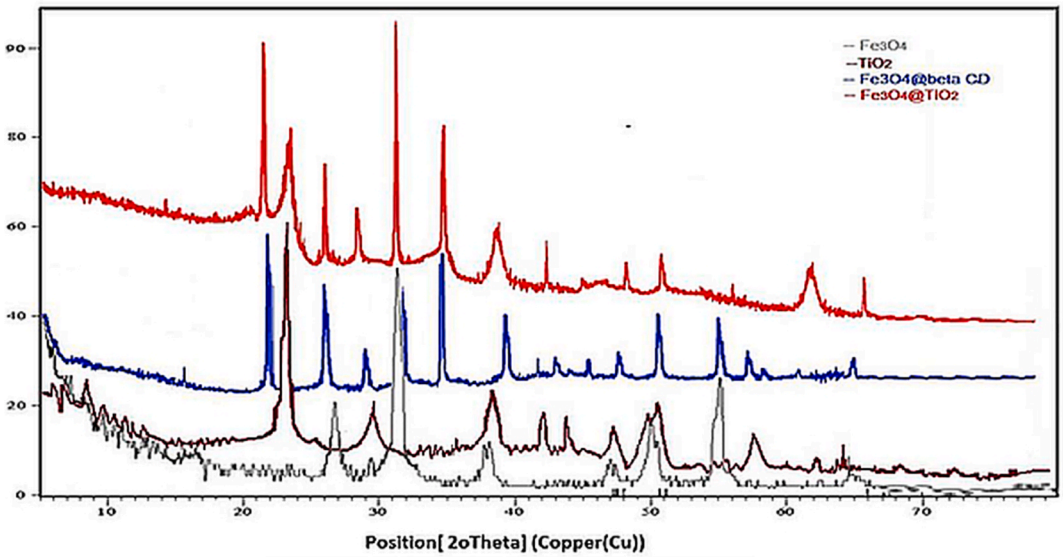

Fig. 2. XRD patterns of (a) Fe_3O_4, (b) TiO_2, (c) Fe_3O_4@β-CD and (d) TiO_2/Fe_3O_4.

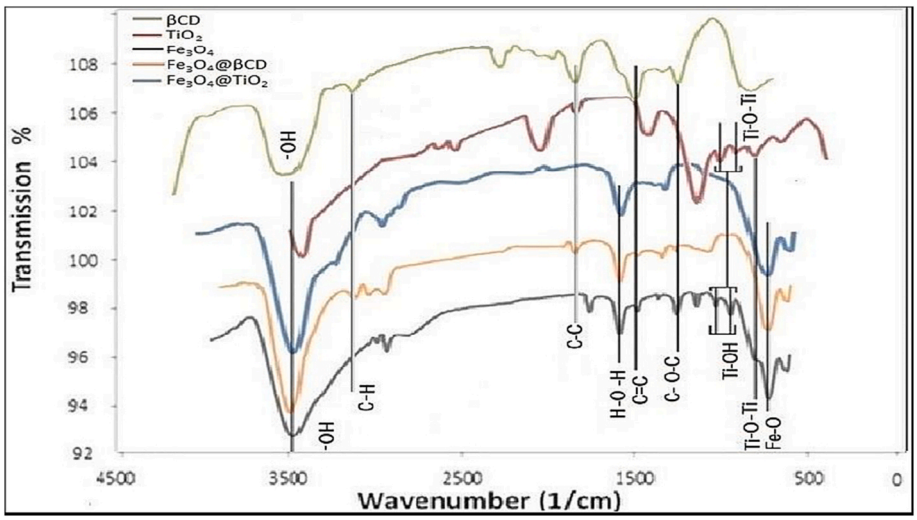

Fig. 3. FTIR spectrum for: a-β-cyclodeztrin, b-TiO_2, c- Fe_3O_4, d- Fe_3O_4@βCD and e– Fe_3O_4@TiO_2 nanoparticles and nano composite.

nanocomposite, followed by a 15 % weight loss from 140 to 248 °C attributed to the two-stage dissociation of β-bonding organic groups. In contrast, Fe_3O_4/TiO_2 exhibited a 5.78 % weight loss from 70 to 185 °C due to water evaporation and oxidation of magnetite to hematite, followed by a 5.2 % weight loss between 183 and 485 °C attributed to the transformation of remaining maghemite particles into hematite. Finally, a minimal weight loss of 0.71 % was observed from 485 to 800 °C, indicating molecular stability at higher temperatures.

These results suggest that Fe_3O_4@TiO_2 exhibits greater thermal stability compared to Fe_3O_4@β-CD. This enhanced stability could be attributed to stronger bonding between Fe_3O_4 and TiO_2, or to the formation of a protective TiO_2 layer on the surface of the Fe_3O_4 nanoparticles [23].

The thermal stability of Fe_3O_4@/TiO_2 is crucial for its potential applications as a nanocatalyst, particularly in high-temperature catalytic reactions. A thermally stable nanocatalyst can maintain its activity under elevated temperatures, which is essential for many industrial processes. Indeed, the TGA results indicate that Fe_3O_4@TiO_2 is a promising nanocatalyst with favorable thermal stability characteristics [24].

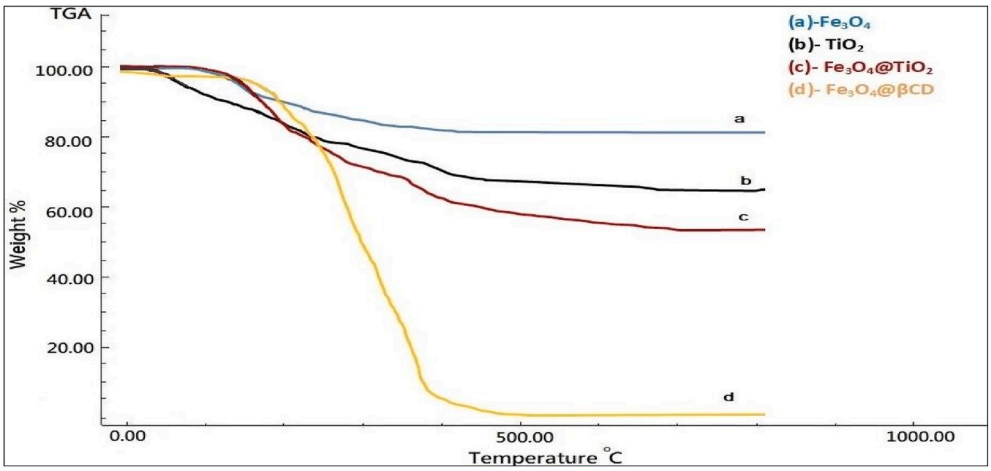

Fig. 4. TGA (thermogravimetric analysis) for nanomaterials bar: (a)-Fe_3O_4, TiO_2 and Nano composites: (c)-Fe_3O_4@Tio_2 and (d)-Fe_3O_4@βCD

3.5. Adsorption capacities for heavy metals at different concentration of Fe_3O_4@ β-cyclodextrin (mg/L) at different PH values at ambient temperature

The adsorption capacity of Fe_3O_4@β-cyclodextrin for heavy metals showed a consistent increase with rising pH, as evidenced by the data presented in Tables 1–3. This trend can be attributed to the increasing negative charge on the Fe_3O_4@β-cyclodextrin surface at higher pH values, enhancing the electrostatic attraction towards positively charged metal ions. Notably, Table 3 demonstrated the highest adsorption capacities, with copper exhibiting the maximum value (149.81 mg/g), followed by nickel (69.14 mg/g), lead (56.44 mg/g), and cadmium (36.88 mg/g). These variations in adsorption capacities likely stem from the different affinities of these metals for the Fe_3O_4@β-cyclodextrin surface. The superior adsorption capacity for Cu can be explained by the stronger affinity between Cu ions and the β-cyclodextrin rings. Cyclodextrins are known to form stable inclusion complexes with various organic and inorganic molecules, including metal ions. The particularly stable inclusion complex formed between Cu ions and cyclodextrin rings accounts for the higher adsorption capacity observed for Cu compared to the other three pollutants, aligning with previous findings in the literature [25].

Fe_3O_4@ β-cyclodextrin is also a material that shows promise for the adsorption of heavy metals from wastewater treated by industry. Adsorption capacity may be influenced by a variety of parameters, such as the characteristics of the pollutant, such as size, charge, and solubility, and the characteristics of the adsorbent, such as surface area, porosity, and chemical composition. Fe_3O_4 nanoparticles are frequently employed as adsorbents to remove different types of contaminants from wastewater that is utilized in industry. Fe_3O_4 nanoparticles provide chemical processes an active surface, which catalyzes the reaction. Because of their enormous surface area, Fe_3O_4 nanocomposites offer additional surface area for catalytic processes. The outcomes concur with the results that have been reported [26,27].

3.6. Adsorption capacities for heavy metals at different concentration of Fe_3O_4@ TiO_2 (mg/L) values at ambient temperature at different PH

Results presented in Tables 4–6 reveal the adsorption capacity of Fe_3O_4@TiO_2 for various heavy metal pollutants at different pH levels and ambient temperature. Following a similar trend to the results shown in Tables 1–3, the adsorption capacity increases with increasing pH for all pollutants.

Likewise, Copper showed the highest adsorption capacity (160.5 mg/g), followed by nickel, lead, and cadmium (77.09, 56.0, 46.05 mg/g) (Figs. 5–7). This is likely due to the different affinities of these metals for the surface of Fe_3O_4@TiO_2 The adsorption capacity of Fe_3O_4@TiO2 for all pollutants is higher than that of Fe_3O_4@β-cyclodextrin, probably due to the different surface properties of the two materials. Furthermore, the results suggest that Fe_3O_4@TiO_2 is a promising material for the adsorption of heavy metals from industrial

Table 1
Adsorption capacities for at concentration 20 mg/L heavy metals (mg/g) at different PH values at ambient Temperature.

PH at ambient temperature	Lead (Pb)	Nickel (Ni)	Cadmium (Cd)	Copper (Cu)
2	33.65 ± 0.225	52.43 ± 1.03	17.61 ± 0.051	113.56 ± 1.66
4	36.08 ± 0.173	56.4 ± 0.876	20.04 ± 0.077	119.1 ± 1.42
6	37.01 ± 0.209	58.71 ± 1.11	23.27 ± 0.12	133.7 ± 2.16
8	37.77 ± 0511	63.05 ± 0.744	27.25 ± 0.085	141.05 ± 2.03
10	33.7 ± 0.261	61.7 ± 1.07	19.11 ± 0.14	122.3 ± 1.72

LSD 6.6.

Table 2
Adsorption capacities for at concentration 30 mg/L heavy metals (mg/g) at different PH values at ambient temperature.

PH at ambient temperature	Lead (Pb)	Nickel (Ni)	Cadmium (Cd)	Copper (Cu)
2	38.22 ± 0.155	52.88 ± 0.65	20.1 ± 0.187	117.01 ± 1.76
4	41.18 ± 0.118	58.12 ± 0.47	25.5 ± 0.23	124.6 ± 2.07
6	45.76 ± 0.063	63.2 ± 0.38	29.07 ± 0.311	128.9 ± 1.53
8	48.05 ± 023	66.08 ± 0.61	34.12.±0.168	146.31±l.92
10	33.7 ± 0.191	61.7 ± 1.07	19.96.±0.22	126.0 ± 1.88

LSD 7.62.

Table 3
Adsorption capacities for at concentration 40 mg/L heavy metals (mg/g) at different PH values at ambient temperature.

PH at ambient temperature	Lead (Pb)	Nickel (Ni)	Cadmium (Cd)	Copper (Cu)
2	43.065 ± 0.065	58.1 ± 0.023	23.5 ± 0.062	121.31 ± 1.06
4	47.31 ± 0.031	64.36 ± 0.056	28.1 ± 0.028	128.07 ± 1.23
6	52.1 ± 0.07	67.0 ± 0.021	34.41 ± 0.061	135.16 ± 1.09
8	56.44 ± 0.048	69.14 ± 0.173	36.88.±0.09	149.87±l.34
10	48.3 ± 0.112	62.88 ± 0.07	21.07.±0.064	126.86 ± 1.52

LSD 7.93.

Table 4
Adsorption capacities for at concentration 20 mg/L heavy metals (mg/g) at different PH values at ambient temperature.

PH at ambient temperature	Lead (Pb)	Nickel (Ni)	Cadmium (Cd)	Copper (Cu)
2	37.88 ± 0.08	54.12 ± 0.087	25.21 ± 0.14	121.07 ± 2.05
4	38.56 ± 0.031	58.03 ± 0.049	26.87 ± 0.181	126.4 ± 2.16
6	40.21 ± 0.06	65.2 ± 0.141	29.02 ± 0.22	138.9 ± 1.88
8	43.02 ± 0.013	67.34 ± 0.076	36.08 ± 0.166	148.67 ± 1.79
10	36.44 ± 0.04	57.88 ± 0.18	26.03 ± 0.28	130.4 ± 1.64

LSD 6.89.

Table 5
Adsorption capacities for at concentration 30 mg/L heavy metals (mg/g) at different PH values at ambient temperature.

PH at ambient temperature	Lead (Pb)	Nickel (Ni)	Cadmium (Cd)	Copper (Cu)
2	37.23 ± 0.11	61.08 ± 0.31	25.89 ± 0.245	123.43 ± 1.22
4	41.06 ± 0.18	63.12 ± 0.46	29.34 ± 0.64	129.1 ± 1.48
6	45.33 ± 0.08	69.0 ± 0.37	32.1 ± 0.38	144.04 ± 1.16
8	51.3 ± 0.24	72.15 ± 0.32	41.55 ± 0.202	152.3 ± 1.28
10	43.26 ± 0.26	59.62 ± 029	30.17 ± 0.55	132.07 ± 1.09

LSD 8.22.

Table 6
Adsorption capacities for at concentration 40 mg/L heavy metals (mg/g) at different PH values at ambient temperature.

PH at ambient temperature	Lead (Pb)	Nickel (Ni)	Cadmium (Cd)	Copper (Cu)
2	39.03 ± 0.76	62.9 ± 0.56	27.01 ± 0155	131.01 ± 2.13
4	45.16 ± 1.01	66.42 ± 0.46	33.5 ± 0.24	135.1 ± 1.85
6	48.28 ± 1.032	74.11 ± 0.28	37.26 ± 0.28	153.0 ± 2.04
8	56.0 ± 0.654	77.09 ± 0.77	46.05 ± 0.171	160.5 ± 1.79
10	42.76 ± 1.11	61.87 ± 0.83	33.01 ± 0.131	136.11 ± 2.03

LSD 10.06.

wastewater [28].

In addition, Fe_3O_4@TiO_2 has demonstrated greater effectiveness in removing a wider range of heavy metals compared to Fe_3O_4@β-cyclodextrin. This superior performance can be attributed to TiO_2's ability to interact with heavy metals through various mechanisms, including electrostatic attraction, chemisorption, and ion exchange [29].

Data illustrated in Figs. 4–6 reveal that the removal efficiency (catalytic activity) of Fe_3O_4@BCD for lead (Pb), nickel (Ni), cadmium (Cd), and copper (Cu) at concentrations ranging from 20 mg/L to 40 mg/L. The removal efficiency is measured as the percentage of pollutants removed from industrial wastewater.

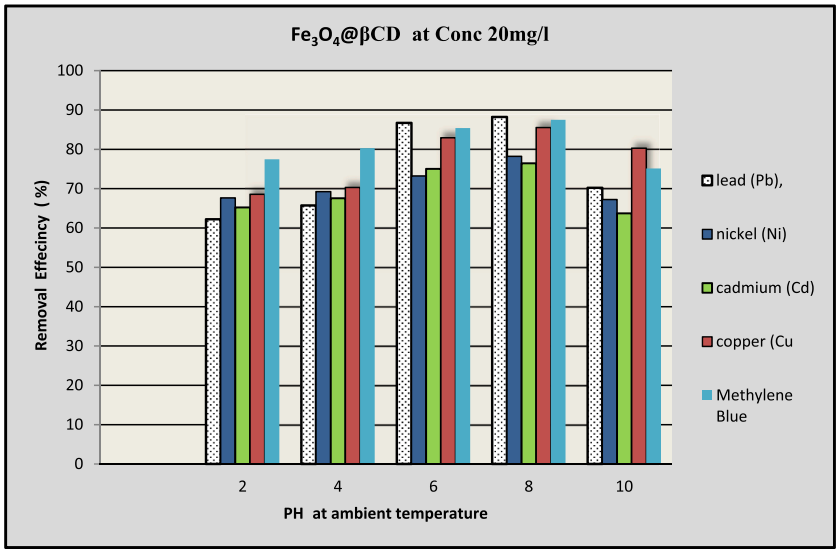

Fig. 5. Removal Efficiency (%) using Fe_3O_4@βCD at 20 mg/l

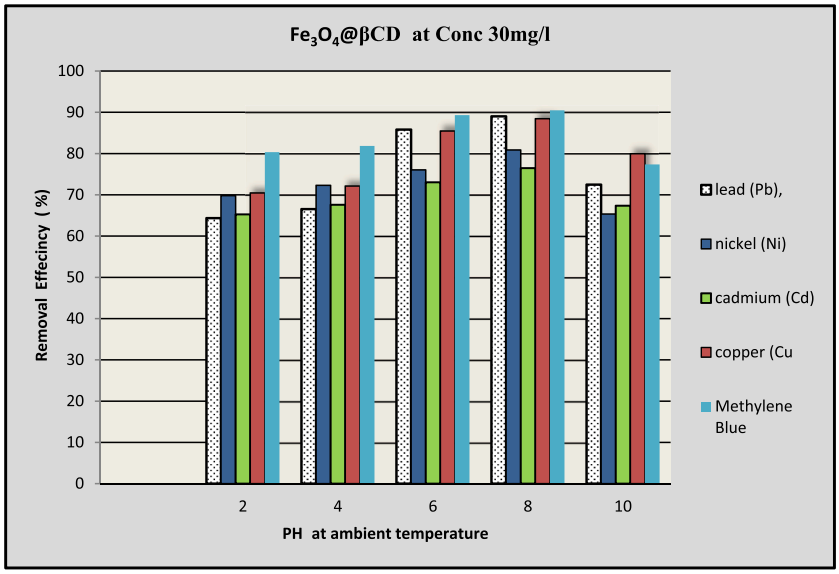

Fig. 6. Removal Efficiency (%) using Fe3o4@βCD at 30 mg/l

The removal efficiency (catalytic activity) of Fe_3O_4@BCD varies depending on the pH and chemical reaction with pollutants. The highest removal efficiency is observed for Methylene Blue (91.16 %) followed by lead (90.50 %), copper (90.48 %), nickel (83.34 %), and cadmium (77.58 %). This suggests that Fe_3O_4@BCD is more effective at removing lead and copper than nickel and cadmium at a concentration of 40 mg/L. Finally, the graph revealed that Fe_3O_4@BCD is a promising material for the removal of chemical pollutants from the industrial wastewater [30].

3.7. Photocatalytic activity of nanocatlysit composites: removal efficiency (%) of nanocatlysit composite (Fe_3O_4@TiO_2) for heavy metals and dyes

According to results from Figs. 8–10, Fe_3O_4@TiO_2 at 40 mg/L demonstrated the highest removal efficiency among all photocatalysts across various pH and temperature conditions. The removal efficiency of Fe_3O_4@TiO_2 at 40 mg/L remains relatively stable under different pH and temperature conditions, indicating that it is a promising photocatalyst for the removal of pollutants from wastewater. The high and stable removal efficiency at different pH and temperature conditions. The high and stable removal efficiency of Fe_3O_4@TiO_2 at 40 mg/L is likely due to the synergistic effect between Fe_3O_4 and TiO_2. Fe_3O_4, a magnetic material, can help

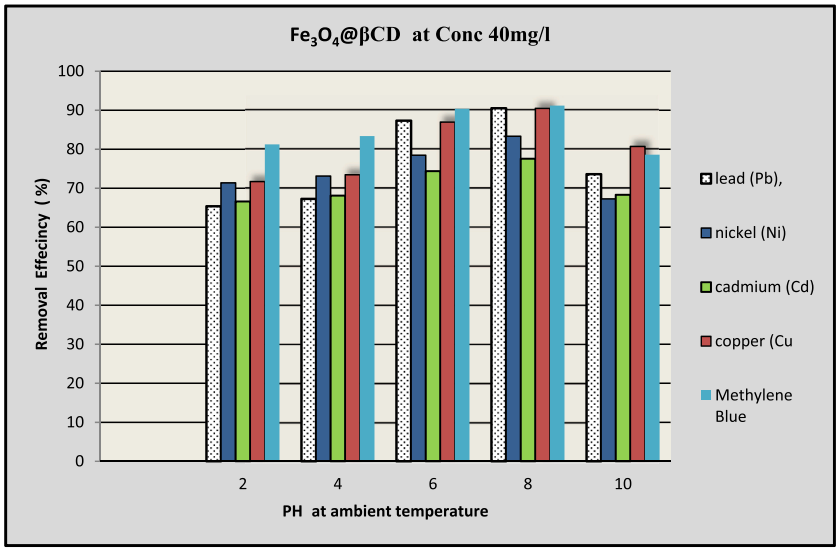

Fig. 7. Removal Efficiency (%) using Fe_3O_4@βCD at 40 mg/l

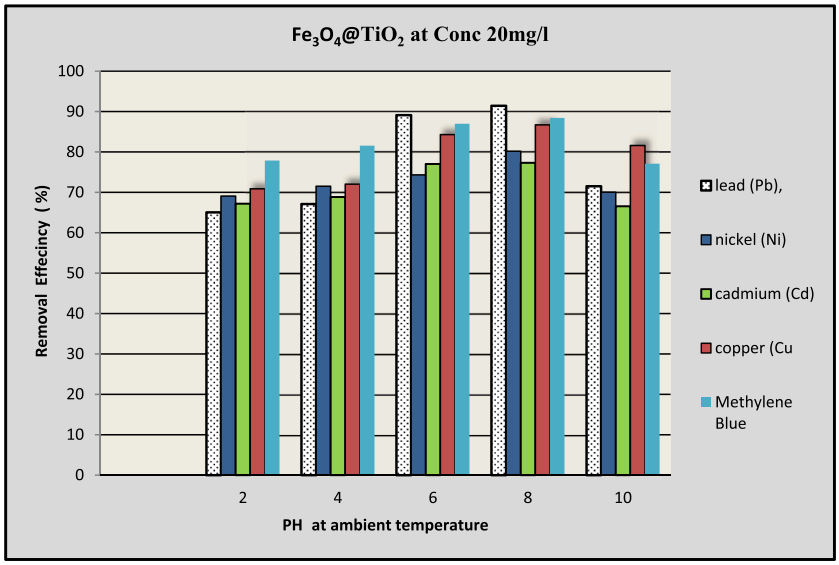

Fig. 8. Removal Efficiency (%) using Fe_3O_4@TiO_2 at 20 mg/l

concentrate pollutants on the surface of the nanocatalyst. TiO2, a semiconductor, can generate photocatalytic reactive oxygen species (ROS) under sunlight irradiation. These ROS can then oxidize and degrade the pollutants.

The synergistic effect between Fe_3O_4 and TiO_2 is also responsible for the stability of the removal efficiency across different pH and temperature conditions. Fe_3O_4 is a basic material, while TiO_2 is acidic material. This combination allows the Fe_3O_4@TiO_2 surface to maintain a relatively neutral pH even when the solution is acidic or basic. This is significant because the photocatalytic activity of TiO_2 is highest at neutral pH [27]. Fe_3O_4@TiO_2 at 40 mg/L proves to be a promising photocatalyst for the removal of pollutants from wastewater, demonstrating high and stable removal efficiency under various pH and temperature conditions [31].

3.8. Catalytic activity mechanism

TiO_2 absorbs photons of light with energy greater than its band gap (3.2 eV). This energy excites electrons from the valence band to the conduction band, creating electron-hole pairs. The electrons in the conduction band react with adsorbed oxygen molecules to form superoxide radicals ($O^{2-\bullet}$). These superoxide radicals then react with organic pollutants, degrading them into carbon dioxide and water (Fig. 11). Simultaneously, the holes in the valence band react with adsorbed water molecules to form hydroxyl radicals ($OH^{\bullet}$)

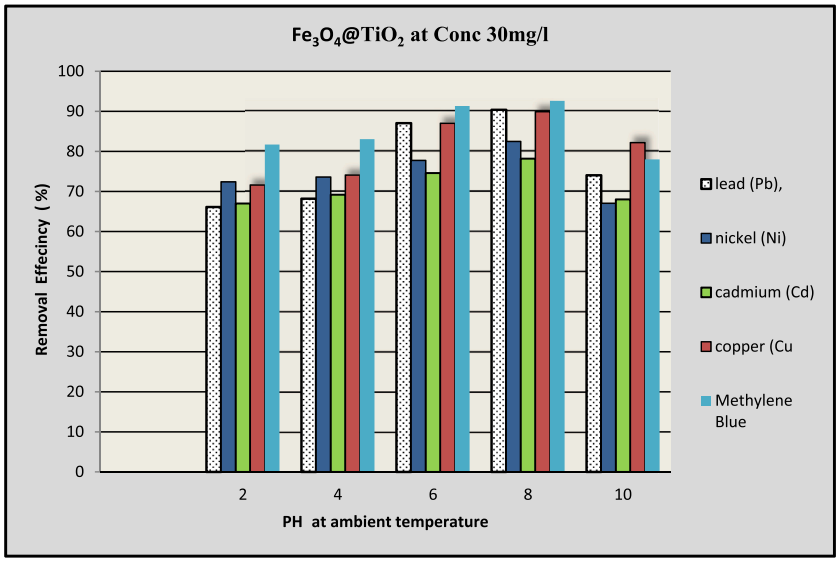

Fig. 9. Removal Efficiency (%) using Fe_3O_4@TiO_2 at 30 mg/l

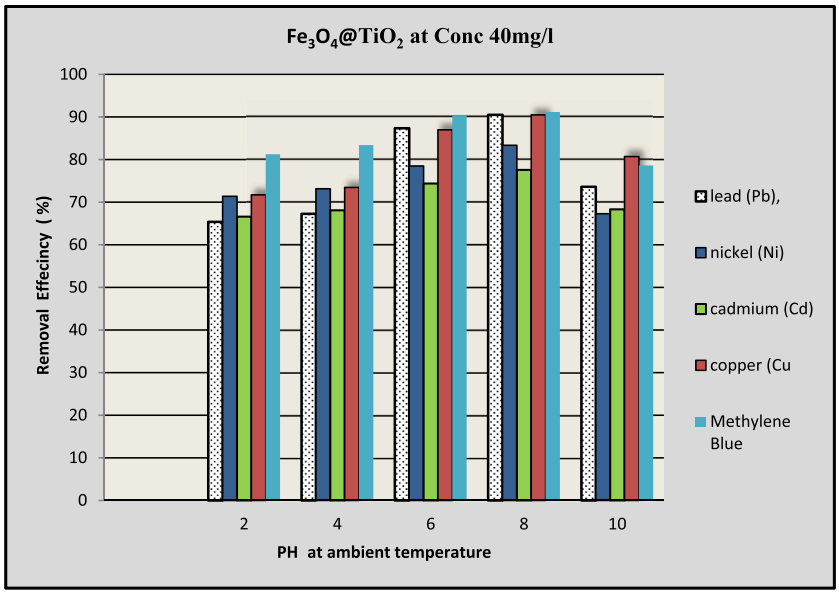

Fig. 10. Removal Efficiency (%) using Fe_3O_4@TiO_2 at 40 mg/L.

[32].

The hydroxyl radicals are highly reactive and can also degrade organic pollutants. Metal ions and dye molecules are adsorbed onto the surface of Fe_3O_4@TiO_2. The Fe_3O_4 nanoparticles absorb photons of light with energy greater than the band gap of TiO_2 (3.2 eV). This energy excites electrons from the valence band of TiO_2 to the conduction band, creating electron-hole pairs. The electrons in the conduction band of TiO_2 then react with adsorbed oxygen molecules to form superoxide radicals ($\bullet O^{2-}$). These superoxide radicals react with protons in water to form hydroxyl radicals ($OH^{\bullet}$).

The hydroxyl radicals are highly reactive and can degrade metal ions and dyes. This degradation of metal ions and dyes by Fe_3O_4@TiO_2 is a promising photocatalytic process for environmental remediation. Fe_3O_4@TiO_2 photocatalysts can be used to purify water as well as air, and to degrade pollutants on surfaces [33].

4. Conclusion

The synthesis method of engineered nanocatalyst materials significantly enhanced their stability and applicability across various

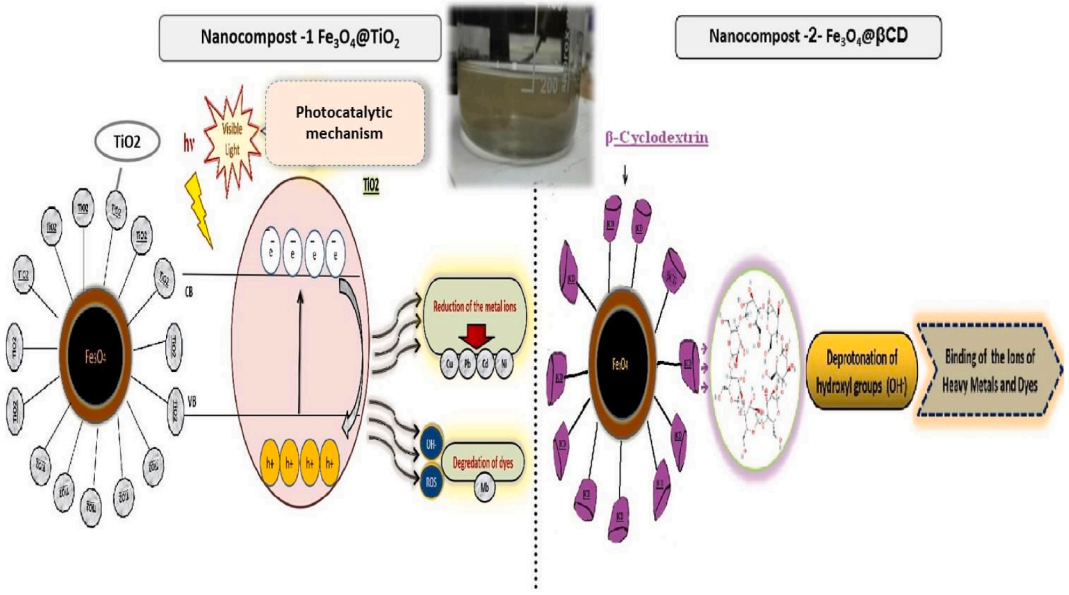

Fig. 11. Catalytic activity mechanism for Catalytic and photocatalytic of tow Nano composites: Fe_3O_4@βCD and Fe_3O_4@TiO_2

environmental conditions. The use of tetraethylammonium hydroxide, rather than conventional bases like ammonia or sodium hydroxide, improved the stability of magnetite (Fe_3O_4) and prevented its transformation into bulk form. Combining β-cyclodextrin with magnetite increased the compound's efficiency in attracting and absorbing pollutant ions and heavy metals. Similarly, the magnetite (Fe_3O_4) and titanium dioxide (TiO_2) composite at 40 mg/L concentration demonstrated remarkable photocatalytic performance. While both compositions yielded promising results, the titanium-based composite is recommended for future applications. These findings have potential for large-scale industrial implementation, where the volume of wastewater can inform the preparation of appropriate concentrations of nanoformulations.

Funding

No specific financial support was received for this research from any public, commercial, or non-profit funding agency.

Data availability statement

Data will be made available on request.

CRediT authorship contribution statement

Safer Tale Almutairi: Writing – review & editing, Writing – original draft, Resources, Project administration, Methodology, Investigation, Funding acquisition, Formal analysis, Data curation, Conceptualization.

Declaration of competing interest

The authors declare that they have no known competing financial interests or personal relationships that could have appeared to influence the work reported in this paper.

Acknowledgments

The author would like to extend his gratitude to the Deanship of Scientific Research at the University of Hafr Al Batin in Saudi Arabia for their continuous support of this research.

References

[1] S.T. Khan, A. Malik, Engineered nanomaterials for water decontamination and purification: from lab to products, J. Hazard Mater. 363 (2019) 295–308.
[2] Z. Aghalari, et al., Effectiveness of wastewater treatment systems in removing microbial agents: a systematic review, Glob. Health 16 (1) (2020) 13.
[3] B. Bethi, et al., Nanomaterials-based advanced oxidation processes for wastewater treatment: a review, Chemical Engineering and Processing - Process Intensification 109 (2016) 178–189.

[4] N. Ahmadpour, M. Nowrouzi, V. Madadi Avargani, M.H. Sayadi, S. Zendehboudi, Design and optimization of TiO2-based photocatalysts for efficient removal of pharmaceutical pollutants in water: recent developments and challenges, J. Water Proc. Eng. 57 (2024) 104597, https://doi.org/10.1016/j.jwpe.2023.104597.
[5] S. Singh, et al., Applications of nanoparticles in wastewater treatment, in: R. Prasad, et al. (Eds.), Nanobiotechnology in Bioformulations, Springer International Publishing, Cham, 2019, pp. 395–418.
[6] D. Lopez-Tejedor, R. Benavente, J.M. Palomo, Iron nanostructured catalysts: design and applications, Catal. Sci. Technol. 8 (7) (2018) 1754–1776.
[7] A. Akbarzadeh, M. Samiei, S. Davaran, Magnetic nanoparticles: preparation, physical properties, and applications in biomedicine, Nanoscale Res. Lett. 7 (1) (2012) 144.
[8] B. Wu, et al., Study on corrosion resistance and photocatalysis of cobalt superhydrophobic coating on aluminum substrate, Surf. Coating. Technol. 330 (2017) 42–52.
[9] Z. Esania, H. Younesi, M. Nowrouzi, H. Karimi-Maleh, Characterization and assessment of the photocatalytic activity of ZnO-Fe3O4/TiO2 nanocomposite based on MIL-125(Ti) synthesized by mixed solvo-hydrothermal and sol-gel methods, J. Water Proc. Eng. 47 (2022) 102750, https://doi.org/10.1016/j.jwpe.2022.102750.
[10] M. Khalatbary, M.H. Sayadi, M. Hajiani, M. Nowrouzi, S. Homaeigohar, Green, sustainable synthesis of γ-Fe2O3/MWCNT/Ag nano-composites using the viscum album leaf extract and waste car tire for removal of sulfamethazine and bacteria from wastewater streams, Nanomaterials 12 (2022) 2798.
[11] M. Khalatbary, M.H. Sayadi, M. Hajiani, M. Nowrouzi, Adsorption studies on the removal of malachite green by γ-Fe_2O_3/MWCNTs/Cellulose as an eco-friendly nanoadsorbent, Biomass Conversion and Biorefinery 14 (2022) 2495–2513.
[12] I. Castellanos-Rubio, et al., A milestone in the chemical synthesis of Fe3O4 nanoparticles: unreported bulklike properties lead to a remarkable magnetic hyperthermia, Chem. Mater. 33 (22) (2021) 8693–8704.
[13] A. Kubiak, et al., Hydrothermally assisted fabrication of TiO2-Fe3O4 composite materials and their antibacterial activity, Materials 13 (21) (2020) 4715.
[14] Z. Zarnegar, J. Safari, Modified chemical coprecipitation of magnetic magnetite nanoparticles using linear–dendritic copolymers, Green Chem. Lett. Rev. 10 (4) (2017) 235–240.
[15] M. Aliahmad, N. Nasiri Moghaddam, Synthesis of maghemite (γ-Fe 2 O 3) nanoparticles by thermal-decomposition of magnetite (Fe 3 O 4) nanoparticles, Materials Science-Poland 31 (2013) 264–268.
[16] W. Li, R. Liang, A. Hu, Z. Huang, Y. Zhou, Generation of oxygen vacancies in visible light activated one-dimensional iodine TiO2 photocatalysts, RSC Adv. 4 (2014) 36959–36966.
[17] J. Zhang, X. Yu, W. Guo, J. Qiu, X. Mou, A. Li, et al., Construction of titanium dioxide nanorod/graphite microfiber hybrid electrodes for a high performance electrochemical glucose biosensor, Nanoscale 8 (17) (2016) 9382–9389.
[18] J. Jitputti, et al., Synthesis of TiO2 nanotubes and its photocatalytic activity for H2 evolution, Jpn. J. Appl. Phys. 47 (1S) (2008) 751.
[19] S. Salamat, H. Younesi, N. Bahramifar, Synthesis of magnetic core–shell Fe3O4@TiO2 nanoparticles from electric arc furnace dust for photocatalytic degradation of steel mill wastewater, RSC Adv. 7 (31) (2017) 19391–19405.
[20] M. Abbas, B.P. Rao, V. Reddy, C. Kim, Fe3O4/TiO2 core/shell nanocubes: single-batch surfactantless synthesis, characterization and efficient catalysts for methylene blue degradation, Ceram. Int. 40 (7) (2014) 11177–11186.
[21] A. Banisharif, S. Hakim Elahi, A. Anaraki Firooz, A. A Khodadadi, Y. Mortazavi, TiO2/Fe3O4 nanocomposite photocatalysts for enhanced photo-decolorization of Congo red dye, Int. J. Nanosci. Nanotechnol. 9 (4) (2013) 193–202.
[22] H.N.A.M. Sakinah, C. Rohaida (Eds.), Characterization of β-cyclodextrin Complexes with Natural Dye. National Conference on Postgraduate Research (Ncon-Pgr09), 2009.
[23] M. Stoia, R. Istratie, C. Păcurariu, Investigation of magnetite nanoparticles stability in air by thermal analysis and FTIR spectroscopy, J. Therm. Anal. Calorim. 125 (3) (2016) 1185–1198.
[24] L.A. Cobos Cruz, et al., Synthesis of magnetite nanoparticles–β-cyclodextrin complex, J. Alloys Compd. 466 (1) (2008) 330–334.
[25] V.K. Yadav, et al., Synthesis and characterization of amorphous iron oxide nanoparticles by the sonochemical method and their application for the remediation of heavy metals from wastewater, Nanomaterials 10 (8) (2020) 1551.
[26] F. Fu, Q. Wang, Removal of heavy metal ions from wastewaters: a review, J. Environ. Manag. 92 (3) (2011) 407–418.
[27] C. Liosis, et al., Heavy metal adsorption using magnetic nanoparticles for water purification: a critical review, Materials (Basel) 14 (24) (2021).
[28] P. Kumari, et al., Cyclodextrin-based nanostructured materials for sustainable water remediation applications, Environ. Sci. Pollut. Control Ser. 27 (26) (2020) 32432–32448.
[29] R. Sinha, P.S. Ghosal, A comprehensive appraisal on status and management of remediation of DBPs by TiO2 based-photocatalysts: insights of technology, performance and energy efficiency, J. Environ. Manag. 328 (2023) 117011.
[30] S.E.Z. Syeda, et al., Recent advancements in cyclodextrin-based adsorbents for the removal of hazardous pollutants from waters, Polymers 14 (12) (2022) 2341.
[31] V. Mirkhani, et al., Photocatalytic degradation of azo dyes catalyzed by Ag doped TiO2 photocatalyst, J. Iran. Chem. Soc. 6 (3) (2009) 578–587.
[32] H. Du, et al., Formation and mechanisms of hydroxyl radicals during the oxygenation of sediments in Lake Poyang, China. Water Research 202 (2021) 117442.
[33] S.J. Armaković, M.M. Savanović, S. Armaković, Titanium dioxide as the most used photocatalyst for water purification: an overview, Catalysts 13 (1) (2023) 26.